This is a repository copy of *Evolution of coronal jets during Solar Cycle 24*.

White Rose Research Online URL for this paper:
https://eprints.whiterose.ac.uk/211261/

Version: Published Version

CrossMark

# Evolution of Coronal Jets during Solar Cycle 24

Sz. Soós[1,2] , J. Liu (刘佳佳)[3,4] , M. B. Korsós[1,2,5] , and R. Erdélyi[1,2,6]

[1] Department of Astronomy, Eötvös Loránd University, Pázmány Péter sétány 1/A, H-1112 Budapest, Hungary; jiajialiu@ustc.edu.cn, robertus@sheffield.ac.uk
[2] Hungarian Solar Physics Foundation, Petőfi tér 3, H-5700 Gyula, Hungary
[3] Deep Space Exploration Lab/School of Earth and Space Sciences University of Science and Technology of China, Hefei, 230026, People's Republic of China
[4] CAS Key Laboratory of Geospace Environment, Department of Geophysics and Planetary Sciences University of Science and Technology of China, Hefei, 230026, People's Republic of China
[5] Dipartimento di Fisica e Astronomia "Ettore Majorana", Università di Catania, Via S. Sofia 78, I 95123 Catania, Italy
[6] Solar Physics & Space Plasma Research Center (SP2RC), School of Mathematics and Statistics, University of Sheffield, Hounsfield Road, S3 7RH, UK

## Abstract

The focus of this study is on the spatial and temporal distributions of 2704 solar jets throughout Solar Cycle 24, from beginning to end. This work is a follow-up paper by Liu et al. With this extended data set, we have further confirmed the two distinct distributions of coronal jets: one located in polar regions and another at lower latitudes. Further analysis of the series of coronal jets revealed kink oscillations of the global solar magnetic field. Additionally, studying the northern and southern hemispheres separately showed an antiphase correlation that can be interpreted as a global sausage oscillatory pattern of the loci of the coronal jets. We also investigated how the variability of the solar cycle may impact the power law index of coronal jets by dividing the data set into the rising and declining phases of Solar Cycle 24. However, there is no compelling evidence to suggest that the power law index changes after the maximum. It is worth noting that based on this vast database of solar jets, the degradation of the 304 Å channel of the Atmospheric Imaging Assembly instrument on board the Solar Dynamics Observatory can also be identified and confirmed. Finally, we searched for compelling signatures of the presence of active longitude in the coronal jet database. There was no obvious evidence with a high probability of an active longitude; therefore, this question remains yet to be addressed further.

*Unified Astronomy Thesaurus concepts:* Solar coronal transients (312); Solar activity (1475); Solar cycle (1487); Solar extreme ultraviolet emission (1493); Solar oscillations (1515); Active solar corona (1988)

## 1. Introduction

Solar coronal jets are one of the typical, frequent, localized, and highly dynamic phenomena in the solar atmosphere. Although they are quite common, they are less intense than solar flares. On the other hand, they may transport a considerable amount of mass, momentum, and energy across the solar atmosphere. Coronal jets are elongated plasma ejections (Demastus et al. 1973; Brueckner & Bartoe 1978) that occur in the upper atmosphere of the Sun (for a more comprehensive review about coronal jets, see Raouafi et al. 2016). Coronal jets can be detected in various wavelengths, including UV/EUV, X-rays (Shibata et al. 1992; Tsiropoula et al. 2012; Raouafi et al. 2016), white light (Wang & Sheeley 2002; Kudriavtseva & Prosovetsky 2019), and Hα (Shen et al. 2012; Qi et al. 2022).

Coronal jets, as shown by Liu et al. (2023), also exhibit a power-law distribution of their frequency just as solar and stellar flares (Crosby et al. 1993; Benz & Krucker 1999; Parnell & Jupp 2000; Shibayama et al. 2013; Cliver et al. 2022). The physical mechanism responsible for the eruption of solar coronal jets is believed to be magnetic interchange reconnection between closed and open magnetic field lines (Shibata et al. 1992; Canfield et al. 1996; Shibata et al. 2007; Moore et al. 2010; Pariat et al. 2015). Though the physics behind this power-law distribution needs to be explored, it was suggested by Liu et al. (2023) that they are essential evidence that coronal

jets, different classes of flares (Lu & Hamilton 1991), and coronal mass ejections (CMEs, Lamy et al. 2019) are likely triggered by the same underlying physical process.

Many of the solar features also show different solar cycle variations. The most well-known one is the 11 yr activity cycle, among others. This 11 yr solar cycle is present in the properties of various features (e.g., appearance, size, etc.) of sunspots, flares, coronal holes, total solar irradiance, and so on (Solanki & Krivova 2011). Furthermore, whether the Sun features a North–South asymmetric behavior of sunspots, flares, etc., during solar cycles is still a matter of debate. Roy et al. (2020) studied the hemispheric asymmetry of the solar flare index, among others, for Solar Cycle 24. They observed that these asymmetric characteristics in the northern and southern hemispheres vary during the progression of the solar cycle (e.g., Solar Cycle 24 shows south-dominated characteristics). Janardhan et al. (2018) argued that the southern solar hemisphere unambiguously reversed polarity before the maximum of Solar Cycle 24. El-Borie et al. (2021) summarized in detail which hemisphere was dominated by, e.g., sunspot number, solar radio flux, and solar mean magnetic field in Solar Cycle 24. All these studies (and others not mentioned here) inspire us to raise the question: do the physical parameters and properties of the localized jets also follow solar cyclic variations?

To identify localized coronal jets among the wealth of solar features is not an easy task. There have been several works born in the past regarding coronal jets, where the jets were identified manually. Manually searching for coronal jets is a time-consuming and laborious task. However, recently Liu et al. (2023) developed a novel semiautomated identification

algorithm of off-limb coronal jets (SAJIA) and applied it to the observations of the Atmospheric Imaging Assembly (AIA) on board the Solar Dynamics Observatory (SDO). They found that the coronal jets (i) are spatially located mostly along the equatorial and polar regions; (ii) in Solar Cycle 24, more coronal jets were found in the southern polar region; (iii) migrate from higher latitudes toward the equator; (iv) exhibit changes in properties with a period around 11 months; and (v) present a power-law index of thermal energy almost identical to solar and stellar flares and CMEs.

To confirm and refine what Liu et al. (2023) found, this work now extends their approach by applying a more extensive set of diagnostics to a larger number of jets. Therefore, our aims are to (i) map the fine structure of the jet distribution, (ii) search for solar cycle variation in the characteristic parameters of the jets, and (iii) further support (or refute) the existence of the conjecture of active longitude with analyzing jets. Our aims will be realized by the objectives of (i) advancing the currently available jet database[7] from its 6 hr cadence to 3 hr temporal resolution for the entire SDO timeline (2010–2022), i.e., double the data points. Then, (ii) critically assess/confirm the newly detected jets. Next, (iii) transfer the jet coordinates to Carrington coordinates with B0 angle correction. Correct the intensity, width, height, and area of the jets in the database, and (iv) determine and analyze the power-law index changes as a function of time, which will give us information about the nature of the underlying driver mechanism(s) of the formation of the jets.

In this work, we investigate a total of 2704 coronal jets and apply additional methods, e.g., the Gaussian Mixture Model (Pedregosa et al. 2011) and the Lomb–Scargle Periodogram (Astropy Collaboration et al. 2013, 2018, 2022). The selection criteria for the studied jets are listed in Section 2. Section 3 describes the methods and presents the analysis of the main findings of our work, which are summarized and discussed in Section 4.

## 2. Data Processing

### 2.1. Method

For our analysis, the data provided by the Solar Dynamics Observatory/Atmospheric Imaging Assembly (SDO/AIA, Lemen et al. 2012) instrument at the 304 Å were applied. The semiautomated identification algorithm of off-limb coronal jets (SAJIA) to automatically detect jets was used, as presented by Liu et al. (2023).

SAJIA was applied to each studied full-disk observation. First, the size of the original observations is reduced to $512 \times 512$ pixels in order to run the code faster. Next, the algorithm fitted a mask with a size 2% larger than the solar disk to cover the disk and small-scale structures above the limb. Therefore, structures smaller than $\sim$10 Mm cannot be detected (e.g., spicules). A binary map is also generated for each single image to make it easier to detect structures on the limb. In the end, the code is searching for contours that can be covered by elongated rectangles that most resemble coronal jets. Furthermore, SAJIA does not take into account elongated contours which are (i) at an angle of less than $60°$ to the local perpendicular, (ii) the ratio of axes of these contours being less than 1.5, and (iii) not on the limb. The detected contours are

then checked manually to validate that they are real. It is worth noting that there is a minor error in determining the length of the jets because the original SDO images were downgraded to $512 \times 512$ pixels; consequently, the resolution was reduced to $3.5$ Mm px$^{-1}$. Also because of the mask applied, there is no possible way to detect coronal jets below approximately 10 Mm, as a result. As there is only a subcategory of all coronal jets that were detected, we refer to them as coronal jets detected by SAJIA from now on.

### 2.2. Data

The same parameters and settings were used to expand the existing coronal jet database detected by SAJIA. Now, we collected additional data from 2010 June 1 to 2020 May 31 at four further time stamps daily at 3, 9, 15, and 21 hr, which were not yet included in the former database composed of times 0, 6, 12, and 18 hr. Then, the data were further expanded from 2020 May 31 to 2021 December 31, with detections at eight time stamps (0, 3, 6, 9, 12, 15, 18, 21 hr) each day. As a result, the previous 6 hr cadence is now improved to a 3 hr temporal resolution. There were some data gaps, mostly because of maintenance issues and Lunar transits. Due to this issue, there are a total of 109 missing observation points where there was no data available. Also, due to maintenance operations at 21:00:00, the images of the 304 Å channel are not available; therefore, data at 21:00:28 were used instead. After SAJIA was applied for the extended range of the data, we manually checked each candidate to confirm and validate whether it was a real or false detection, following the criteria defined by Liu et al. (2023).

Furthermore, we were rather strict about accepting a jet candidate as a real detection. Namely, when there was a jet 30 minutes earlier than a given time stamp, but the same jet was not visible at this time stamp, only some other warm plasma that the jet detection script marked as a jet, then such data was marked as a false jet. Similarly, if another warm plasma was detected at a one-time stamp, but the real jet was a few degrees away, then it was marked as a false detection as well. Initially, with the jet detection algorithm, a total of 4227 jet candidates were found during the newly examined period. Based on the criteria above, 1489 turned out to be real jets, while the remaining 2601 were false detections. Furthermore, in 42 cases, we could not conclude whether it was a jet or not. In addition to the 109 gaps in the database, there were also 95 cases where, although there was a measurement during the examined time stamp by AIA, there was no data before or after a given time stamp. Therefore we could not verify manually in several consecutive images, whether the object was a jet or not. The coronal jets identified by year are summarized in Table 1. For our further study, in addition to the 1489 jets listed above, all the 1215 jets found by Liu et al. (2023) are also included. In total, we have now 2704 true jets detected by SAJIA in our coronal jet catalog. In the final catalog, (i) the Stonyhurst coordinates of each jet were converted to Carrington Coordinates with B0 angle correction, (ii) the intensity of each jet was corrected, and (iii) the real size of the jets was determined. The intensity of the jets was corrected after the automatic detection to amend the CCD degradation, as can be seen in Liu et al. (2023).

---

**Table 1**
Newly Detected Coronal Jets

| | No. of Candidates Detected | True Jets | False Jets | Unsure Jets | No Images Were Found |
|---|---|---|---|---|---|
| 2010 | 592 | 319 | 225 | 3 | 45 |
| 2011 | 787 | 338 | 432 | 10 | 7 |
| 2012 | 615 | 202 | 404 | 3 | 6 |
| 2013 | 643 | 181 | 445 | 11 | 6 |
| 2014 | 502 | 126 | 352 | 5 | 19 |
| 2015 | 283 | 108 | 171 | 4 | 0 |
| 2016 | 168 | 52 | 112 | 4 | 0 |
| 2017 | 100 | 32 | 67 | 1 | 0 |
| 2018 | 83 | 25 | 57 | 0 | 1 |
| 2019 | 106 | 26 | 73 | 0 | 7 |
| 2020 | 145 | 37 | 105 | 0 | 3 |
| 2021 | 203 | 43 | 158 | 1 | 1 |
| Total | 4227 | 1489 | 2601 | 42 | 95 |
| | | 35.23% | 61.53% | 0.99% | 2.25% |

**Note.** Coronal jet database, without the jets already detected by Liu et al. (2023). From 2010 June 1 to 2020 May 31, jets were identified at four time stamps (3, 9, 15, 21). From 2020 May 31 to 2021 December 31, eight time stamps (0, 3, 6, 9, 12, 15, 18, 21) were applied.

## 3. Analysis

During the manual check, we noticed that the images became grainier as one progresses through time. This is due to the fact that the sensitivity of the SDO/AIA passbands degraded over time. Possible causes include the deposition of organic molecules from the telescope structure onto the optical elements and the decrease in detector sensitivity following (E)UV exposure. Boerner et al. (2012) modeled the change in transmission as a function of time, and the table of correction parameters is publicly available at the Joint Science Operations Center (JSOC; Scherrer et al. 2010). To correct our data sample, the `get_correction_table` function of the `aiapy.calibrate` Python package (The SunPy Community et al. 2020) is applied. Also, the `degradation` function from the same package is applied to compensate for the degradation over time. In Table 2, these functions were employed to determine how much the 304 Å channel deteriorated over the years.

The traces of SDO/AIA 304 Å channel degradation can be clearly seen in Table 1. The first column shows the number of jet candidates found by the algorithm. In 2010, we only have measurements starting from 2010 June 1, when SDO went into service mode. This happened shortly after the minimum of the solar cycle, i.e., at the start of the Solar Cycle 24. Although there were more detections in the following years (2011–2013), in terms of proportions, the number of jets found was not as high as expected. The number of detected jets continues to decrease until the maximum of the Solar Cycle 24 (2014–04). Toward the end of the Cycle, the number of detected jets dropped rather drastically. Then, this trend is followed by a
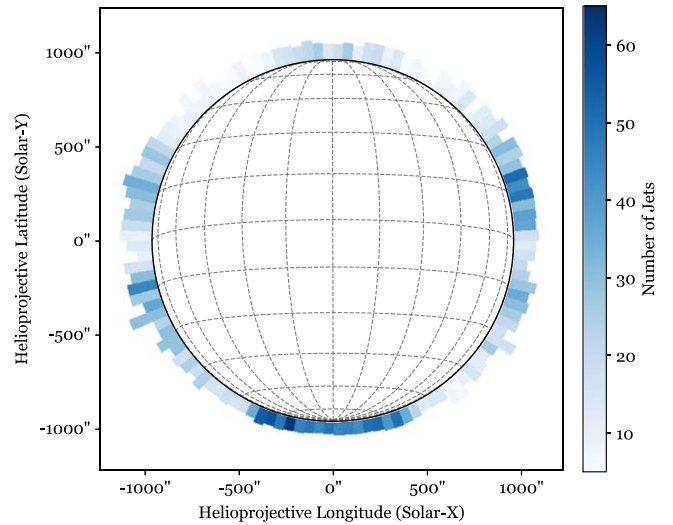


**Figure 1.** Distribution of the coronal jets of the combined SAJIA database for the entire studied interval between 2010 June 1 to 2021 December 31. The white disk represents the solar disk. The length of each blue colored bar was determined as the mean of the length of the coronal jets in the given 3° interval and multiplied by two for easier visibility. The shade of blue is the number of jets detected in each interval.

**Table 2**
SDO/AIA 304 Å Channel Degradation Factor

| Year | Degradation Factor |
|---|---|
| 2010-06-01 | 0.892 |
| 2011-01-01 | 0.557 |
| 2012-01-01 | 0.309 |
| 2013-01-01 | 0.368 |
| 2014-01-01 | 0.271 |
| 2015-01-01 | 0.149 |
| 2016-01-01 | 0.095 |
| 2017-01-01 | 0.079 |
| 2018-01-01 | 0.063 |
| 2019-01-01 | 0.055 |
| 2020-01-01 | 0.055 |
| 2021-01-01 | 0.055 |

**Note.** 304 Å channel is experiencing rapid deterioration over time.

slight increase indicating the start of Solar Cycle 25. The decline in the number of detected jets has already been seen since 2011. This is confirmed by the fact that starting from 2011, the ratio of true and false jets is reversed. Furthermore, this ratio continues to deteriorate over the years in favor of the false jets. In total, about 61.53% of the 4227 jets were found to be false detection.

### 3.1. Distribution of Coronal Jets

In Figure 1, one can see the spatial distribution of the coronal jets detected by SAJIA as a function of the position angle. The large sample of data enables an unbiased insight into the distribution of the jets. From Figure 1, the location of the jets
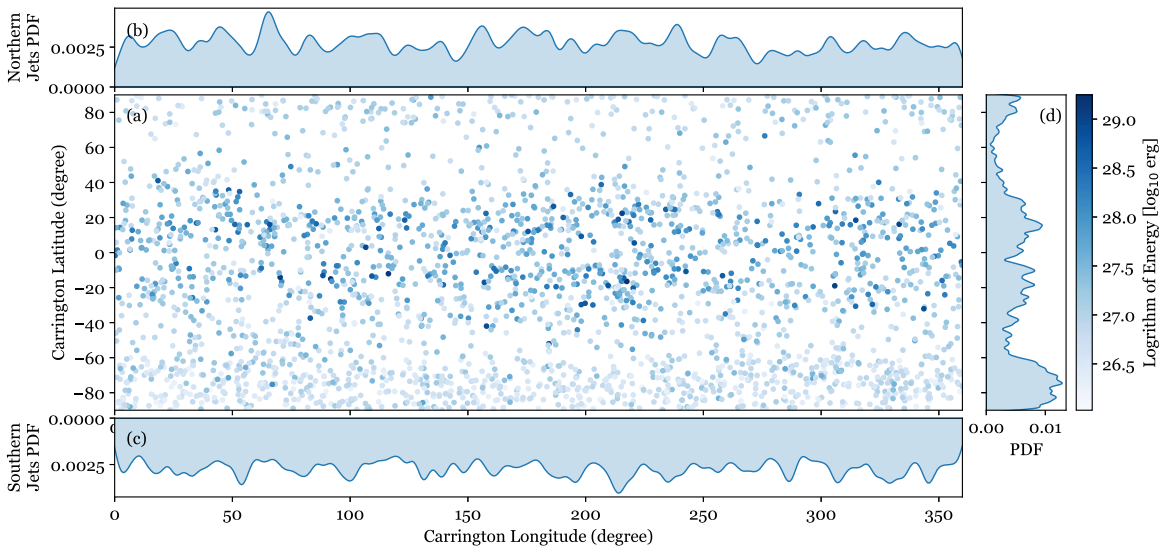
**Figure 2.** (a) shows all detected coronal jets represented in Carrington Coordinates from 2010 June 1 to 2021 December 31. The color bar depicts the logarithm of energy. (b) depicts the distribution of the northern jets, while (c) shows the distribution of the southern jets. (d) shows the distribution of jets by latitude.
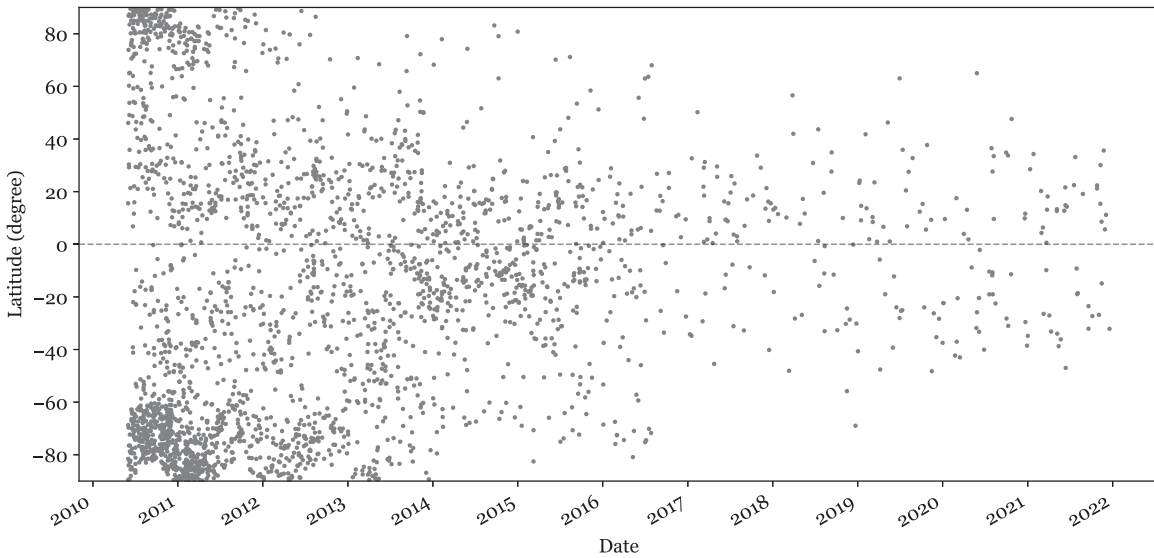


**Figure 3.** Latitude of all detected coronal jets from 2010 June 1 to 2021 December 31.

detected during the entire examined time interval is immediately visible. The following can be found:

1. jets rarely form between $\pm 10°$ latitude,
2. jets tend to concentrate between $\pm 10°$–$30°$ latitude at both sides of the equator, i.e., in the band often populated by active regions,
3. above $\pm 60°$, the density of jets increases significantly at the poles. The greater number of jets visible at the south pole is perhaps due to the asymmetry of the solar mean magnetic field ($|B|$), as El-Borie et al. (2021) state that the southern hemisphere dominated the Solar Cycles 21–24, and,
4. between $\pm 30°$ and $\pm 60°$, the number of jets is negligible compared to the number of jets at low latitudes and polar regions.

In Figure 2(a), all 2704 coronal jets are shown in Carrington coordinates, where the color bar depicts the logarithm of energy in $log_{10}$ erg units. Here, the energy of each jet was estimated as

defined by Liu et al. (2023). Figure 2(b) shows the distribution of the northern jets by longitude, while Figure 2(c) depicts the distribution of the southern jets by longitude. Figure 2(d) shows the distribution of jets by latitude. In Figure 2(d), one can observe a visually strong northern/southern asymmetry between the polar regions. The jets have two independent concentrated distributions. One is in the polar regions, above $\pm 60°$, hereafter referred to as polar jets. The other concentration of distribution is in the band of active regions, which from now on will be referred to as low-latitude jets.

In Figure 3, the latitude coordinates of all coronal jets detected by SAJIA from 2010 June 1 to 2021 December 31 are shown. In this figure, it can also be clearly observed that significantly more jets were formed in the southern hemisphere from 2010 June until approximately 2013. What is immediately obvious is that, in the northern pole, the jets disappeared almost without a trace by 2011–2012. In contrast, in the southern pole, the jets disappear only by 2013–2014. From Table 2, one can see that by 2013–2014, the 304 Å channel degraded to 30%,
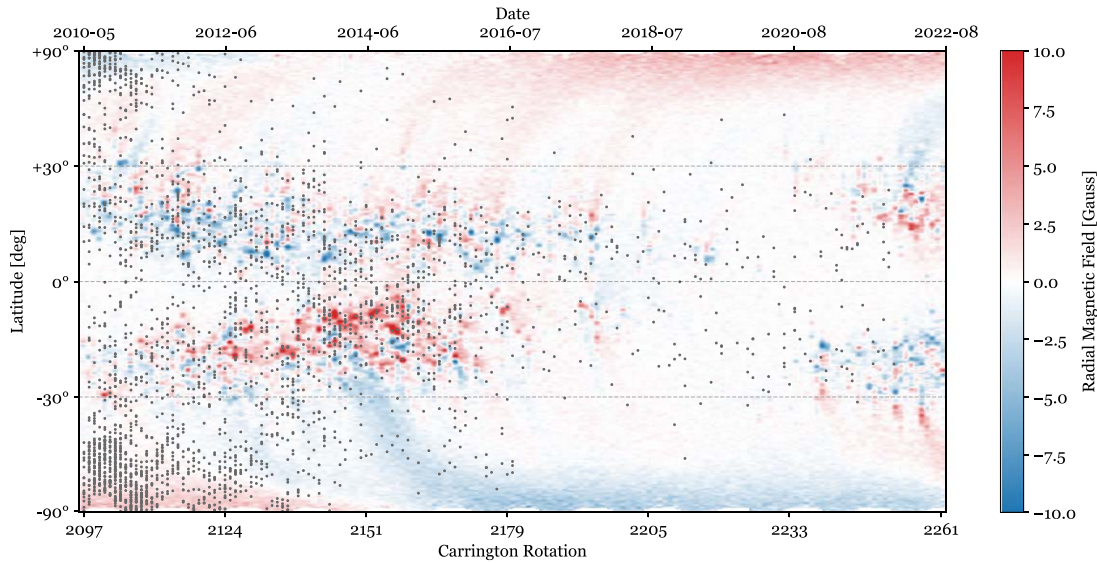
**Figure 4.** Magnetic butterfly diagram as constructed by Hathaway (2015). In the magnetic diagram, the red color corresponds to the positive magnetic flux, while the blue color corresponds to the negative fluxes. Both the positive and negative fields saturate at ±10 G. As the magnetic butterfly diagram, each jet in the longitude direction was integrated into each Carrington rotation and plotted with a gray color.

**Table 3**
Parameters of the Coronal Jets Detected by SAJIA

|  | All Jets | Low-latitude Jets, B0 <60° | Polar Jets, B0 ⩾60° |
|---|---|---|---|
| Number of Jets | 2704 | 1595 | 1109 |
| Intensity Mean (DN) | 96079.1 | 146653.9 | 23341.9 |
| Intensity Max. (DN) | 4801671.5 | 4801671.5 | 496975.3 |
| Intensity Std. (DN) | 263928.9 | 333704.9 | 26722.2 |
| Length Mean (Mm) | 37.4 | 43.8 | 28.1 |
| Length Std. (Mm) | 31.7 | 38.2 | 14.4 |

**Note.** Parameters of the coronal jets broken down into low-latitude and polar regions, based on the extended database.

which explains the disappearance of jets in the southern hemisphere. The question is, why did all this happen earlier in the northern hemisphere? We would like to leave this as an open question, as we do not currently have more data to determine the most likely cause. Furthermore, it can be observed that the low-latitude jets are not affected significantly by the degradation of the CCD.

In Table 3, the basic parameters of the extended database of the coronal jets are shown. The jets have two independent distributions, as revealed earlier, i.e., at the polar regions between ±60°–90° and between lower latitudes. The polar region is characterized by jets of smaller size and lower intensity, but they are more frequent—suggesting that jets form more easily at the poles. On the other hand, the maximum, the mean, and the standard deviation of the intensity of jets in between lower latitudes are an order of magnitude higher, and the average length is more than 10 Mm larger. During the laborious manual inspection, we also experienced that there are many small, filigree jets at the poles, while jets at lower latitudes are more related to some larger activities, e.g., active regions or flares.

In order to connect the formation of the jets with the magnetic field underlying them, the so-called "Magnetic butterfly diagram" (Hathaway 2015) was reconstructed by averaging the radial magnetic field from synoptic maps in the longitude direction for each solar rotation. To reconstruct the magnetic butterfly diagram, as one can see in Figure 4, the hmi.mrsynop_small_720s data product provided by JSOC (SDO/HMI) was used. The x-axis refers to longitude in degrees, and the y-axis is equal steps in sine (latitude). The radial component was selected, which does not distort the magnetic flux as much as the line-of-sight component near the polar regions. First, the individual Carrington Maps were integrated in the direction of longitude. Next, these integrated columns were placed next to each other from CR2097 to CR2261 (156 pieces). The outcome can be seen via the colored background of Figure 4, where the red color corresponds to the positive magnetic flux while the blue depicts the negative counterpart. Both the positive and negative fields saturate equally at ±10 G. Similarly, for the magnetic butterfly diagram, every coronal jet has been added up in the longitude direction in each Carrington rotation. Then, these columns of points were overplotted on the magnetic butterfly diagram with a greyish color. For this reason, it can be seen that the jets take on discrete values. Our extended jet database ends earlier (2021 December 31) than the reconstructed magnetic butterfly
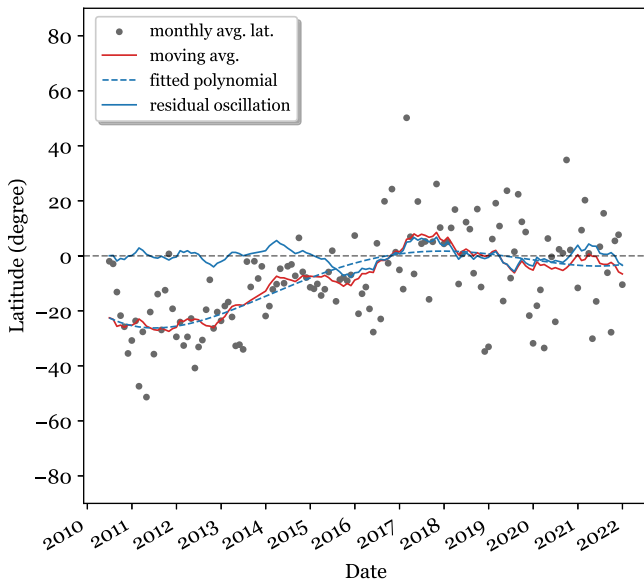
**Figure 5.** Detrended residual oscillation curve of the monthly averaged latitudes of the coronal jets for the two hemispheres together. Detrending was performed using a fourth-order polynomial fit, which was selected based on the best BIC. The gray dots represent the monthly averaged latitudes of the jets. The red curve shows the outcome of the moving average for the gray dots. The dashed blue curve is the fourth-degree polynomial fitted to the solid red curve. The solid blue curve is the residual shape of the oscillation, i.e., the dashed blue curve subtracted from the red solid curve.

diagram (2022 October). Between $-30°$ and $+30°$, one can observe the magnetic flux drifting toward the equator in both hemispheres. On the other hand, above $\pm30°$, a strong magnetic flux drift is observed in the opposite direction to the drift experienced at lower latitudes. These so-called magnetic polar jets[8] transport the magnetic flux in the direction of the poles. Interestingly, the locations of coronal jets do not outline these magnetic polar jets. It looks as if the coronal jets are formed not at the magnetic polar jets but in between them.

### 3.2. Oscillatory Pattern in the Loci of Coronal Jets

Here, in Figure 5, the latitudes of the coronal jets were averaged on a monthly basis using both hemispheres altogether, which is represented by gray dots. Later in the section, the two hemispheres will be analyzed separately. Then, using the monthly averaged latitudes, a 17 month moving average was applied from which the red solid line was constructed. Then, a fourth-degree polynomial was fitted to the red solid line represented by a dashed blue line. The degree of the fitted polynomial was determined by the best Bayesian Information Criterion (BIC) value. Finally, the blue dashed fitted polynomial was subtracted from the red solid curve, from which the residual shape was obtained in the form of an oscillation, visualized as a solid blue curve. The fitted function was subtracted from the red curve so that the smaller oscillations can be seen enhanced more easily. If one now compares the two hemispheres at the same time, the monthly averaged latitudes outline a sinusoidal oscillatory pattern. The entire system exhibits an oscillation, moving up and down together as if it were a kink-type oscillation of a waveguide.

Once the residual oscillation was determined, a Lomb–Scargle periodogram and a wavelet power spectrum (WPS, Figure 6) were applied to the detrended residual oscillation curve. Not surprisingly, both procedures provide the same information consistently. We will not present it here, but the implementation of the Lomb–Scargle periodogram by Vander-Plas & Ivezić (2015) was used to detect and characterize periodic signals in the residual oscillation.

For the WPS (Figure 6), the algorithm of Torrence & Compo et al. (1998) was employed, using the default Morlet wavelet. From the WPS, global power spectra (GPS) are calculated by averaging the WPS over time. For the WPS, the contour lines mark the significance levels: white at 68%, gray at 95%, and black at 98%. We decided to perform wavelet analysis because it gives a good insight into the evolution of a period, while the Lomb–Scargle periodogram cannot. In the wavelet plot, there are some considerable dynamics revealed for the periods. For example, interestingly, shorter periods (around 1 yr) seem to dominate with lower solar activity. In contrast, the longer period (3 yr) appears around the maximum of the solar cycle and increases continuously. A straight line was fitted to the 98% significance contour of the 3 yr period to gain an insight into the scale of growth. The following equation was obtained for the fitted line: period (year) $= (0.054 \pm 0.022) \cdot$ time (year) $+ (3.0 \pm 0.1)$. The "period" starts at 2.7 yr and ends at 10.0 yr after 2010 June 1. The length of the period is 7.3 yr. The period increases from 3.2 yr to 3.5 yr, i.e., it increases by 0.3 yr after its formation.

In Figure 6, from the GPS, one can observe how the periods relate to each other. If we assume that the 3 yr period may be interpreted as the fundamental of a standing oscillation, then the first overtone (if correct to interpret the system as an inhomogeneous resonator) appears around 1.5–1.6 yr, and also the 1 yr period is clearly present, however, unclear of its origin.

After studying the jets in the northern and southern hemispheres concurrently, let us investigate how the jets behave in the northern and southern hemispheres separately. An analysis similar to the previous one was performed for the northern and southern hemispheres as well. In Figure 7, the latitudes of the coronal jets were averaged on a monthly basis, separately for the northern and southern hemispheres. Both findings are marked with gray dots. Then, for the monthly averaged latitudes, a 17 month moving average was applied, and from that, the red solid line was obtained for both hemispheres. Then, a $1/x$ function was fitted to the red solid lines as visualized by a green dashed line for the northern, and a blue dashed line for the southern hemisphere. Next, the green/blue dashed lines fitted by the $1/x$ function were subtracted from the red solid curves, from which the residual shape of the oscillations was obtained as a green/blue solid curve. We will not present it here, but we have also separately fitted (i) a linear, (ii) a polynomial with higher orders up to 15 (the sixth-order polynomial was the best BIC), (iii) a logarithm, and (iv) a differentiation method to the averaged red curves of the northern and southern hemispheres. There is no significant change in the results for all these various fitting choices.

Let us now investigate the two hemispheres at the same time, where the monthly averaged latitudes outline a sinusoidal oscillation, see Figure 5. In contrast, if we consider the northern and southern hemispheres separately (Figure 7), one can see an antiphase correlation between the green/blue residual oscillation curves with a period of approximately 2–2.5 yr. This
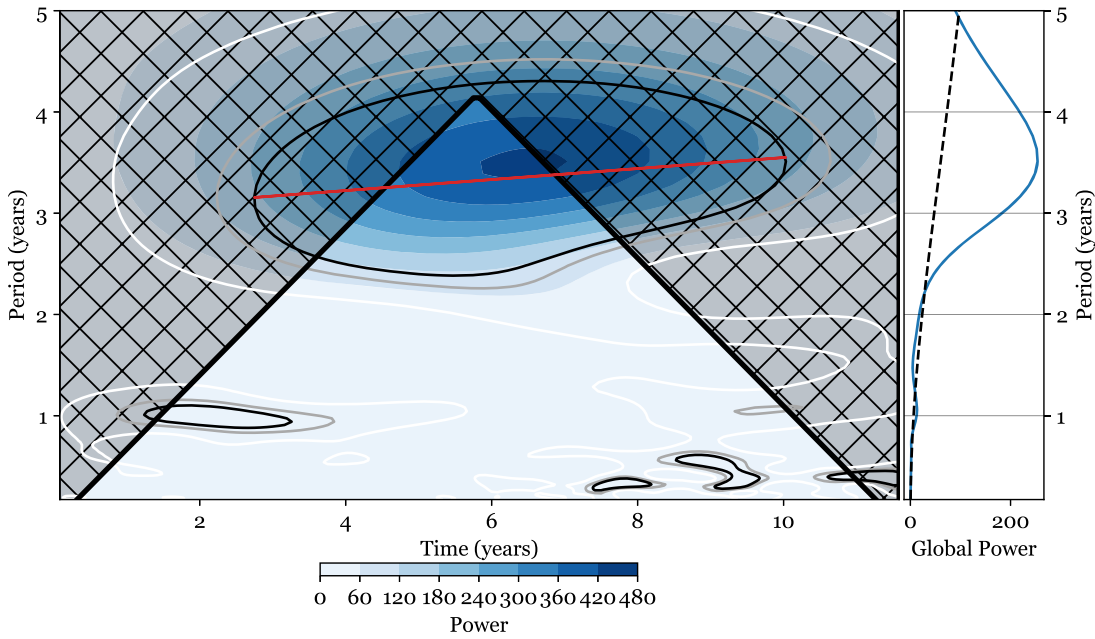
---

[8] By magnetic polar jets, we mean the elongations that appear on the magnetic butterfly diagram, not to be confused with coronal jets.

**Figure 6.** Wavelet analysis of the detrended residual oscillation curve of the monthly averaged latitudes of the coronal jets. The contour lines mark the significance levels (white at 68%, gray at 95%, and black at 98%), while the shaded blue color corresponds to the power, as shown in the color bar. The red line is the result of the fit to the 98% significance contour line. The thick black lines bounding the gridded regions show the cone of influence, i.e., the domain where edge effects become important. The plot to the right of the WPS is the GPS or the time-averaged WPS.
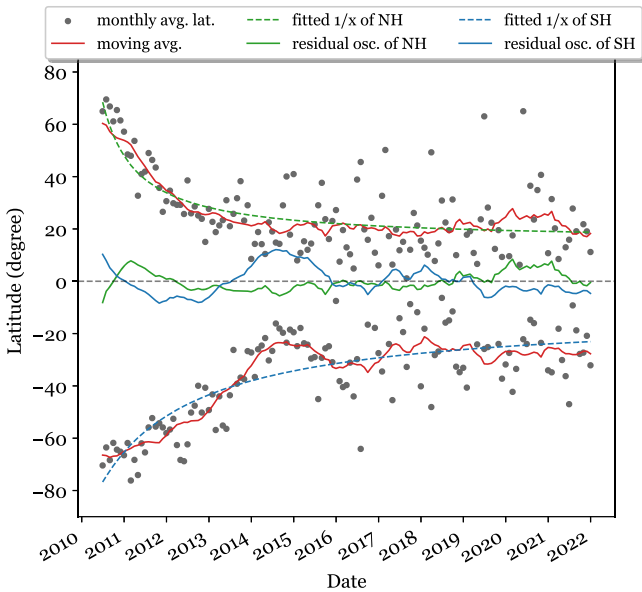


**Figure 7.** Detrended residual oscillation curves of the monthly averaged latitudes of the coronal jets, separately for the northern and southern hemispheres. Detrending was performed using a *1/x* function. The coloring is similar to that shown in Figure 5, with the difference that the green color is for the northern hemisphere and the blue color is for the southern hemisphere jets.

antiphase correlation is always there no matter what background is used to detrend the original signal. This antiphase oscillation, characteristic of the two hemispheres, can also be interpreted as a sausage oscillatory pattern in the birth of these jets. Also, notice that the amplitude of the southern hemisphere detrended latitude oscillation is larger than the one of the northern hemisphere counterpart.

Again, after the residual oscillations were determined, a WPS was applied to the detrended residual oscillation curves, separately for the northern (Figure 8(a)) and southern

(Figure 8(b)) hemispheres. Then, the WPS was applied to the residual oscillations obtained with different detrending functions to find out what kind of periods were found on them. In summary, what we found for the different WPS as fitted with (i) *1/x* function, (ii) a linear, (iii) higher-order polynomials, (iv) a logarithm, and (v) differentiation method:

1. the WPSs look almost identical for the first- and second-order polynomials, *1/x* and differentiation methods,
2. the higher period decreases as we choose a better-fitting function,
3. the best fitting polynomial is the sixth-order polynomial, where the higher period is around 3 yr, and there is also a 1 yr period,
4. the 1 yr period is best seen with the differencing method.

In Figure 7, the amplitude of the southern hemisphere's detrended oscillation is larger than the one of the northern hemisphere, we can also confirm this finding with the GPSs in Figure 8. This finding may support the known northern/ southern asymmetry in solar activity. El-Borie et al. (2021) found that in Solar Cycle 24, (i) sunspot numbers and daily hemispheric sunspot areas have the same level of hemispheric sunspot activity (northern dominance is preferred during the ascending phase of the solar cycle while southern hemispheric dominance has the priority during the descending phase of the solar cycle); (ii) solar radio flux F10.7 has a southern preference by the dominance of 7%; (iii) total solar irradiance has a symmetrical distribution; (iv) plage area has a southern preference by the dominance of 12%; (v) solar flare index has a southern preference by the dominance of 34%; and (vi) solar mean magnetic field ($|B|$) has a southern preference for the Solar Cycles 21–24. It turns out that what we have found with the coronal jets is consistent with these findings and confirms the north/south asymmetry.

We can see the sausage pattern oscillations, with an approximately 4 yr period (but the data series is not long
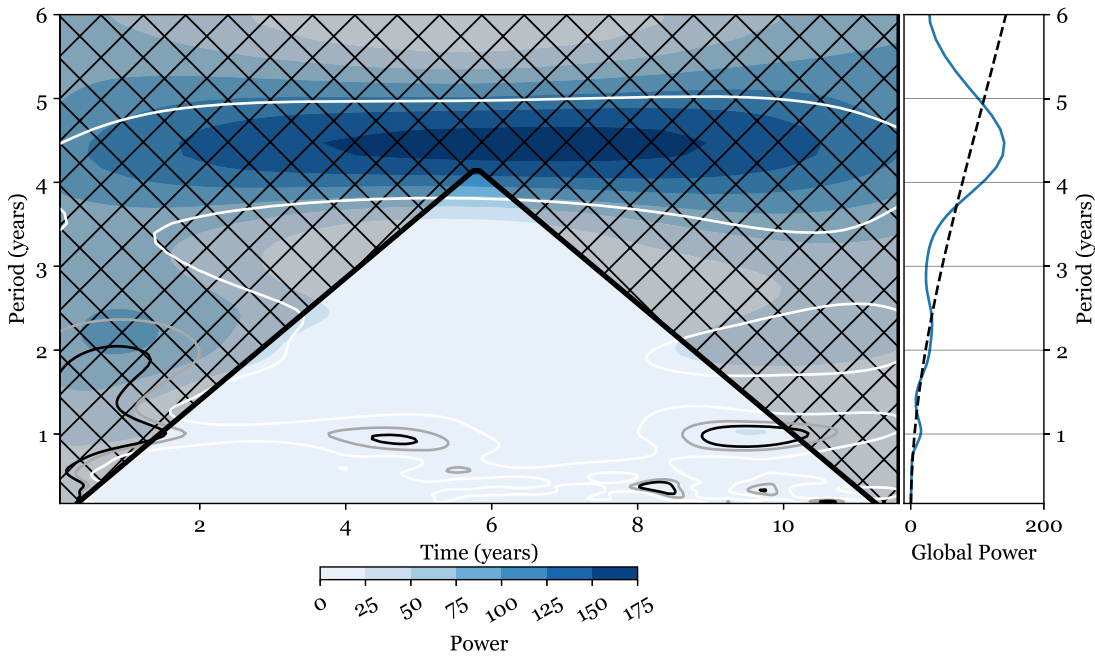
(a)
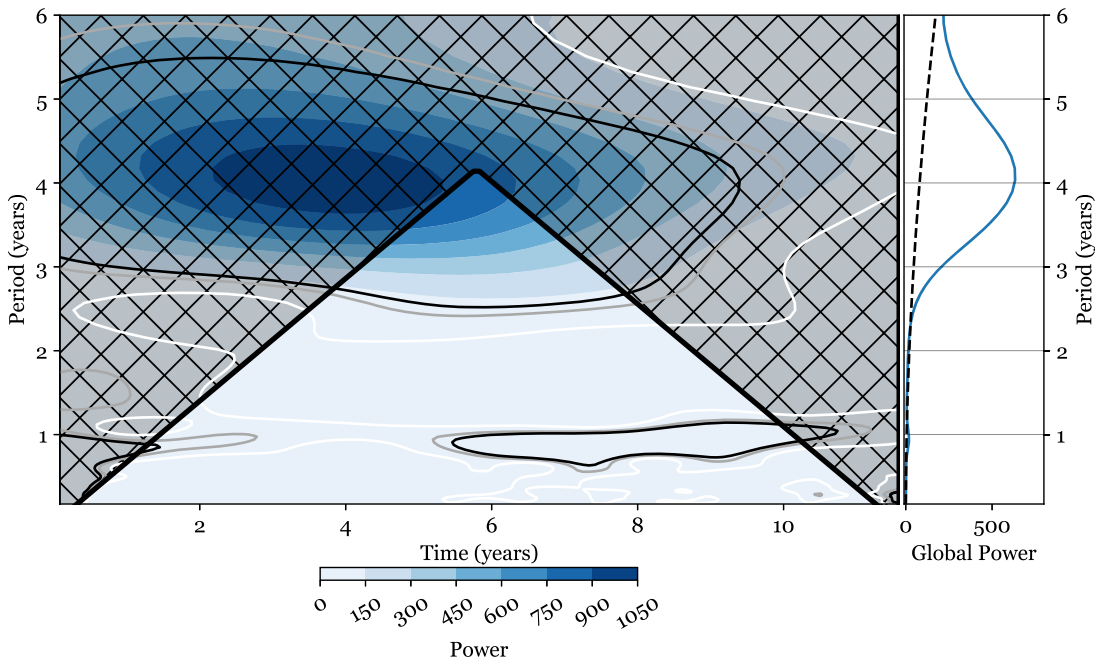


(b)

**Figure 8.** Wavelet analysis of the detrended residual oscillation curves of the monthly averaged latitudes of the coronal jets, separately for the hemispheres. The coloring is similar to that shown in Figure 6. (a) Shows the wavelet analysis of the detrended residual oscillation curve by *1/x* of the monthly averaged latitudes of the northern jets. (b) Similarly for the southern jets.

enough). This is perhaps a consequence of the Sun's compressions as a three-dimensional spherical body since the north and south are not spherically symmetric; asymmetry shows the second order of the oscillation. To the best of our knowledge, similar periods have rarely been reported before.

The following analyses were performed to further confirm the oscillation pattern shown in Figure 5 and Figure 7. In both cases, (i) polar coronal jets above $\pm60°$ were excluded, and (ii) low-latitude coronal jets, i.e., below $\pm60°$ were excluded. In

both cases, the same analysis was performed. Altogether, these analyses fully show this qualitatively, while quantitatively, almost the same results are obtained; i.e., the amplitude, period, and phase of the oscillation do not change considerably.

We have also tested whether the monthly averaging may introduce some errors, which may then hide the true behavior of the data. For this reason, the same analysis was made without the monthly averaging. In summary, we see no significant differences. The same trend was observed for both
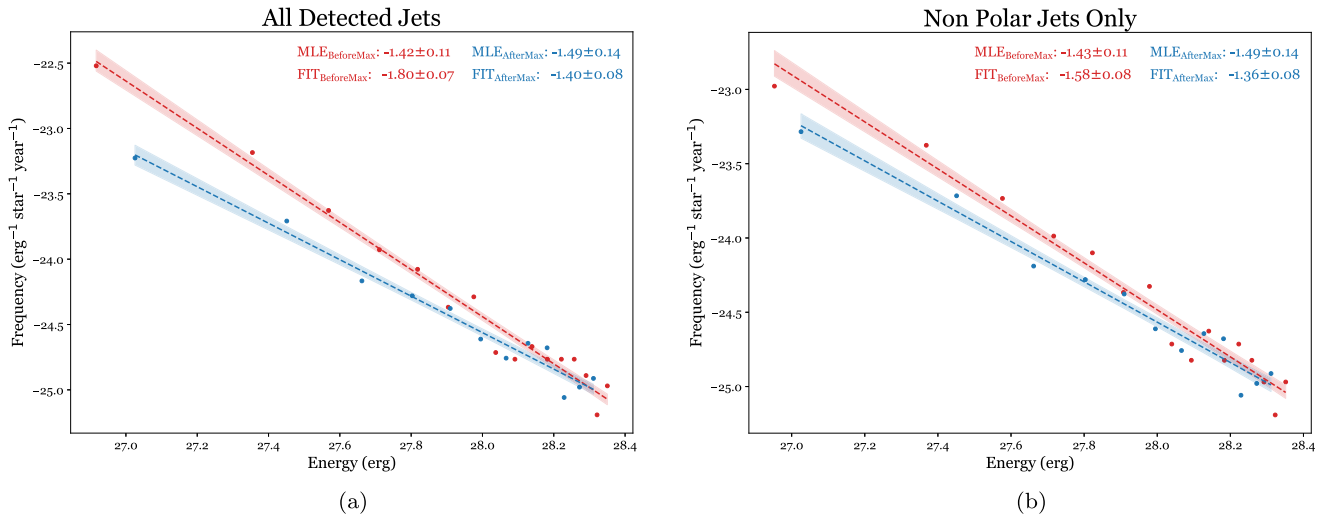
**Figure 9.** Power-law index of coronal jets detected by SAJIA with respect to the solar maximum of Solar Cycle 24. The jets were split into two parts at the maximum of Solar Cycle 24 (2014 April 01). For both figures (a, b), before 2014 April 01, the power law of jets was calculated, shown in red. After 2014 April 01, the power law for the rest of the jets was calculated, shown in blue. (b) A method similar to (a) was applied only to low-latitude jets.

residual curves. Both northern and southern hemispheres have some periodicity, initially 5 yr then followed by 4 yr.

### 3.3. Power Law of Coronal Jets

Next, we analyze how the power-law index of coronal jet distribution changes as a function of time to establish whether the solar cycle variability may influence the power law. This may give us information about the nature of the driver mechanism, which could be local or global heating of the Sun's corona, or it may be a possible marker for a two-cell dynamo of the Sun.

In Figure 9, we show the calculated power law of the distribution of coronal jets. In Figure 9(a), the jets were split into two parts on the date of 2014 April 1, when the second maximum of Solar Cycle 24 appeared. Before 2014 April 1, the power law of 1877 jets was determined, shown in red color. After 2014 April 1, the power law for the rest of the 504 jets was calculated, shown in blue color. One can see quite a significant difference in the fit. Before the maximum, the gradient of the linear fit to the bins is equal to 1.81, but after the maximum, it drops to 1.36. We note that the degradation of the CCD may also play a role here. However, the 504 jets are still a significant amount compared to 1877 to provide a reliable result. On the other hand, the fitting may not always be accurate, and in most cases, the so-called maximum-likelihood estimations (MLE) are more reliable than fitting. It is interesting to note that the MLE indices are almost invariable before and after the solar maximum. This, then, begs the question: is the power law not affected by the solar maximum? This is precisely why we studied the power law by excluding the polar jets (see Figure 9(b)). The same method was applied to the low-latitude jets. What we have already seen is that the power-law indices are not affected by the degradation of the CCD that much. The colors represent the boundary before and after the solar maximum, as in Figure 9(a). In the case where we omit the polar jets, the fitted index is equal to 1.59 before the maximum and equal to 1.31 after the maximum. Again, the margins of error are not overlapping. From this, we conclude that the solar cycle still modulates the formation of jets to some extent. In this case, as previously, the MLE values did not

change significantly. Unfortunately, this suggests that we have not found convincingly strong evidence that the solar cycle affects the power-law index of the distribution of coronal jets. Furthermore, we do not have a very good explanation for this difference in the indices of the fits, and finding one is beyond the scope of the current paper. However, a plausible conjecture may be that there is an overall difference in the energization of the jets between solar minimum and solar maximum.

### 3.4. Hovmöller Diagram of Coronal Jets

In Figure 10, the Hovmöller Diagrams of the coronal jets were constructed. Contrary to Figure 4, every jet in the latitude direction was integrated into each Carrington Rotation. Then, the jets were binned with a 20° sampling window in the longitude direction. Next, these integrated rows were placed on top of each other from CR2097 to CR2261 (156 pieces). This can be seen in the background of Figure 10 with a bluish color bar. Then, we also narrowed down our own Hovmöller Diagrams to match the period studied in Figure 3 of McIntosh et al. (2017). On the left-hand side of Figures 10(a)–(b), the solid blue curves show the number of integrated jets in each Carrington rotation. The solid gray curves show the 13 month smoothed sunspot number, and the solid red curves depict the degradation of the 304 Å channel.

In Figure 10(a), a tilted boundary line is clearly visible there, which separates the less dense (more white) from the higher dense (more blue) regions. This tilted boundary line can also be seen in Figure 3, as the coronal jets in the northern polar region disappear sooner in time than in the southern polar region. Furthermore, ridges inclined at nearly 45° are also visible, where denser and sparser areas change. If these ridges belong to active longitudes (AL, Gyenge et al. 2016), then it could be that as the AL rotates, one observes it as such an inclined ridge as time passes. It seems as if these jets are really clustered in these ridges. Furthermore, the CCD degradation is not that great at that time. A more relevant concern may be that the efficiency of the 304 Å channel decreased to 0.3 by 2012. This is why we observe an anticorrelation of the sunspot number with the number of detected coronal jets. Furthermore, the increasing solar activity and the (E)UV radiation deteriorate the
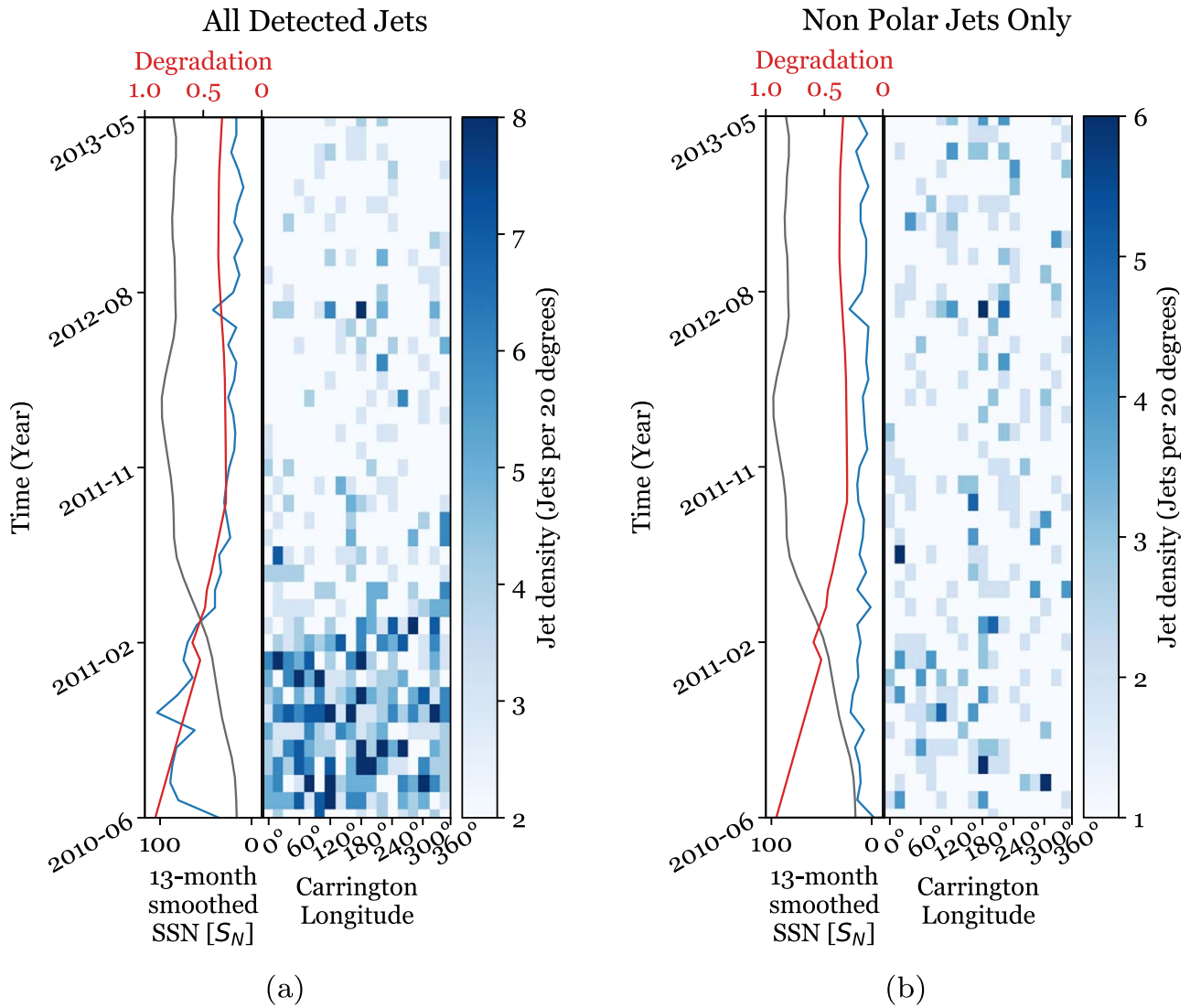
**Figure 10.** Hovmöller Diagrams, the time interval also narrowed down to match the period with Figure 3 in McIntosh et al. (2017). On the left-hand side of Figures 10(a)–(b), the solid blue curves show the number of integrated coronal jets in each Carrington rotation. The solid gray curves show the 13 month smoothed sunspot number, and the solid red curves depict the degradation of the 304 Å channel. The color bar shows the density of the jets every 20° bin. (a) Low-latitude and polar jets binned with 20°. (b) Only low-latitude jets binned with 20°.

CCD even more. For this reason, we omitted the jets in the polar regions (±60°) and constructed Figure 10(b). It can be concluded that, in this case, the tilted boundary line and the ridges disappear. It is also worth noting that the integrated jet number did not change as time progressed.

We report that we did not observe any clustering in the coronal jets detected by SAJIA along the two lines, as found by McIntosh et al. (2017), neither in the case of Figure 10(a) nor in the case of Figure 10(b).

We also performed this study by binning the jets not just with every 20° but also with every 5°, 10°, 15°, 20°, 25°, and 30° for both Figures 10(a)–(b). No significant difference was observed.

### 4. Summary

This work is a follow-up paper by Liu et al. (2023). To detect coronal jets, the novel semiautomated identification algorithm of off-limb coronal jets (SAJIA) was used. The code parameters were unchanged, and the same methodology was followed. The previous existing database has been extended to 2021 December 31; furthermore, the studied time stamps have been doubled. This means that for almost the entire Solar Cycle 24 (from 2010 June 01), a 3 hr resolution database is now established. This extension increased the sample to 2704 coronal jets in the database.[9] For the basic properties of coronal jets detected by SAJIA, we found the following:

1. The degradation of SDO/AIA 304 Å channel is well traced in Table 2. The performance of SAJIA also deteriorates at a similar rate over time, as a consequence, and can be seen in Table 1.
2. The spatial distribution of the coronal jets (Figure 1) confirms the findings of Liu et al. (2023). That is, the jets (i) rarely form between 10° on each side of the equator; and (ii) are typical in two bands in both hemispheres (on the one hand, at low latitudes between ±10°–30°, i.e., in the band of active regions; on the other hand,

---

[9] The data are available at http://space.ustc.edu.cn/dreams/sajia/index.php/.

above $\pm 60°$, i.e., at the poles); and (iii) for Solar Cycle 24, they are more frequent in the southern hemisphere.

3. Figure 2(a) and Table 3 further confirm that there are two independent distributions for the coronal jets. The polar region is characterized by frequent jets of smaller size and lower intensity—suggesting that jets form more easily at the poles. On the other hand, the low-latitude region is dominated by sparser but larger, more energetic jets associated with some major activity, e.g., active regions or flares. Furthermore, these higher energy, larger-sized low-latitude jets are much less sensitive to the degradation of the 304 Å channel.

4. Figure 3 shows the latitude of the coronal jets, which raises the following question: why do jets disappear from the northern polar region a few years earlier than from the southern polar region? We would leave this as an open question for the time being and would need more data to answer it.

5. The formation of the jets connected with the magnetic field underlying them as shown in Figure 4. It can be observed that the location of the coronal jets detected by SAJIA does not coincide with the magnetic polar jets but rather seems to cluster right between them.

Next, we looked for oscillatory patterns in the location of the coronal jets separately for the entire Sun and separately for the two hemispheres. To do this, the latitudes of the jets were averaged on a monthly basis, which were further smoothed by a 17 month moving average. Then the best fitting function by Bayesian Information Criterion was fitted on the smoothed curve. Finally, the fitted function was subtracted from the smoothed curve to obtain the residual oscillation curve.

1. If the two hemispheres are examined simultaneously, then the monthly averaged latitudes outline a sinusoidal oscillatory pattern. The entire system exhibits an oscillation, moving up and down together as if it were a kink-style oscillation, see Figure 5.

2. If the northern and southern hemispheres are examined separately, one can see an antiphase correlation between the northern and southern hemisphere's residual oscillation curves. This antiphase oscillation of the two hemispheres can also be interpreted as a sausage (symmetric) oscillatory pattern, see Figure 7.

Furthermore, a Lomb–Scargle periodogram and a wavelet power spectrum were applied to the detrended residual oscillation curves. In the wavelet plots, there are some considerable dynamics revealed for the periods.

1. Again, when the two hemispheres are examined simultaneously, the shorter periods (around 1 yr) seem to dominate with lower solar activity, see Figure 6. In contrast, the longer period (3 yr) appears around the maximum of the solar cycle and increases continuously. Also, a linear was fitted to the 98% significance contour of the 3 yr period, from which a 0.4 yr increase in period obtained after its formation. If we assume that the 3 yr period may be interpreted as the fundamental of a standing oscillation, then the first overtone appears around 1.5–1.6 yr, and also, the second harmonic is clearly present at 1 yr. However, the origin of it is unclear.

2. When the northern (Figure 8(a)) and southern (Figure 8(b)) hemispheres examined separately, we found that (i) one can observe the sausage pattern oscillations in both hemispheres, with an approximately 4 yr period (to the best of our knowledge this period reported here is rare), and (ii) the amplitude of the southern hemisphere's detrended oscillation is larger than the one of the northern hemisphere which, supporting the known northern/southern asymmetry in solar activity.

The periods show a clear alignment resembling the fundamental, the first harmonic, and the second harmonic of a global standing oscillation (3–4 yr = fundamental, 1.5 yr = first harmonic, 1 yr = second harmonic). These oscillations might represent manifestations of standing modes within the Sun, akin to a three-dimensional elastic spherical (magnetic) body. It is possible that these oscillations are connected to the quasi-biennial oscillations (QBOs; Broomhall & Nakariakov 2015; Kiss & Erdélyi 2018; Kiss et al. 2018) or Rossby waves (Dikpati & McIntosh 2020; Dikpati et al. 2020; Zaqarashvili et al. 2021; Dikpati et al. 2022; Korsós et al. 2023). Then, we further investigated how the solar cycle variability may influence the power law of coronal jets. By splitting the extended jet database into two parts at the second maximum of Solar Cycle 24, i.e., on 2014 April 1, we found the following:

1. If we minimize the effects of the degradation of the SDO/AIA 304 Å channel by looking only at the power law of the low-latitude jets (Figure 9(b)), we find that the power-law index obtained from the fit for before and after the solar cycle maximum is different and beyond the level of the error. However, this estimate may not always be as accurate as the maximum-likelihood estimations. This is why the MLE indices are also calculated before and after the maximum. This latter shows that the MLE indices have not changed significantly. In conclusion, we did not find convincing evidence that the power-law index is changing after the solar cycle maximum.

Finally, we searched for a signature of the active longitude by constructing the so-called Hovmöller Diagrams of the coronal jets. Active longitudes refer to the longitudinal regions where various solar activity phenomena may occur more frequently. We also narrowed down our own Hovmöller Diagrams to match the period studied with Figure 3 of McIntosh et al. (2017). We report that:

1. In Figure 10(a), a tilted boundary line is clearly visible, which can also be seen in Figure 3 as the coronal jets at the northern polar region disappear sooner.

2. We did not observe any clustering in the coronal jets detected by SAJIA along the two lines in Figure 3 as found by McIntosh et al. (2017).

Active longitudes have been the subject of extensive investigation in various aspects. Researchers have studied the longitudinal distribution of sunspots (Warwick 1966; Kitchatinov & Olemskoi 2005; Gyenge et al. 2016), solar flares (Bai 2003), and magnetic bright points (McIntosh et al. 2017). Detecting strong clustering in the longitudinal distribution of coronal jets could potentially support the existence of active longitudes. However, in our analyses, we did not find yet compelling evidence of active longitudes due to the limited data available.

It is known that some solar regions produce homologous jets, with several of them possibly generated within a couple of

hours. While such a region may actually account for a large number of jets, a larger delay in the time stamps used with SAJIA means that only a few jets would be attributed to such a region. The SAJIA method may thus be biased toward underrepresenting such regions. This aspect, however, is beyond the scope of the current paper and would be part of a follow-up study.

## ORCID iDs

Sz. Soós ● https://orcid.org/0000-0002-3606-161X
J. Liu (刘佳佳) ● https://orcid.org/0000-0003-2569-1840
M. B. Korsós ● https://orcid.org/0000-0002-0049-4798
R. Erdélyi ● https://orcid.org/0000-0003-3439-4127

## References

Astropy Collaboration, Price-Whelan, A. M., Lim, P. L., et al. 2022, ApJ, 935, 167
Astropy Collaboration, Price-Whelan, A. M., Sipőcz, B. M., et al. 2018, AJ, 156, 123
Astropy Collaboration, Robitaille, T. P., Tollerud, E. J., et al. 2013, A&A, 558, A33
Bai, T. 2003, ApJ, 591, 406
Benz, A. O., & Krucker, S. 1999, A&A, 341, 286
Boerner, P., Edwards, C., Lemen, J., et al. 2012, SoPh, 275, 41
Broomhall, A. M., & Nakariakov, V. M. 2015, SoPh, 290, 3095
Brueckner, G. E., & Bartoe, J. D. F. 1978, BAAS, 10, 416
Canfield, R. C., Reardon, K. P., Leka, K. D., et al. 1996, ApJ, 464, 1016
Cliver, E. W., Schrijver, C. J., Shibata, K., & Usoskin, I. G. 2022, LRSP, 19, 2
Crosby, N. B., Aschwanden, M. J., & Dennis, B. R. 1993, SoPh, 143, 275
Demastus, H. L., Wagner, W. J., & Robinson, R. D. 1973, SoPh, 31, 449
Dikpati, M., Gilman, P. A., Chatterjee, S., McIntosh, S. W., & Zaqarashvili, T. V. 2020, ApJ, 896, 141
Dikpati, M., Gilman, P. A., Guerrero, G. A., et al. 2022, ApJ, 931, 117
Dikpati, M., & McIntosh, S. W. 2020, SpWea, 18, e02109
El-Borie, M., El-Taher, A., Thabet, A., Ibrahim, S., & Bishara, A. 2021, ChJPh, 72, 1
Gyenge, N., Ludmány, A., & Baranyi, T. 2016, ApJ, 818, 127
Hathaway, D. H. 2015, LRSP, 12, 4
Janardhan, P., Fujiki, K., Ingale, M., Bisoi, S. K., & Rout, D. 2018, A&A, 618, A148
Kiss, T. S., & Erdélyi, R. 2018, ApJ, 857, 113
Kiss, T. S., Gyenge, N., & Erdélyi, R. 2018, AdSpR, 61, 611
Kitchatinov, L. L., & Olemskoi, S. V. 2005, AstL, 31, 280
Korsós, M. B., Dikpati, M., Erdélyi, R., Liu, J., & Zuccarello, F. 2023, ApJ, 944, 180
Kudriavtseva, A. V., & Prosovetsky, D. V. 2019, JASTP, 193, 105039
Lamy, P. L., Floyd, O., Boclet, B., et al. 2019, SSRv, 215, 39
Lemen, J. R., Title, A. M., Akin, D. J., et al. 2012, SoPh, 275, 17
Liu, J., Song, A., Jess, D. B., et al. 2023, ApJS, 266, 1
Lu, E. T., & Hamilton, R. J. 1991, ApJL, 380, L89
McKinney, W. 2010, in Proc. of the 9th Python in Science Conf., ed. Stéfan van der Walt & J. Millman, 56
McIntosh, S. W., Cramer, W. J., Pichardo Marcano, M., & Leamon, R. J. 2017, NatAs, 1, 0086
Moore, R. L., Cirtain, J. W., Sterling, A. C., & Falconer, D. A. 2010, ApJ, 720, 757
Müller, D., Nicula, B., Felix, S., et al. 2017, A&A, 606, A10
Pariat, E., Dalmasse, K., DeVore, C. R., Antiochos, S. K., & Karpen, J. T. 2015, A&A, 573, A130
Parnell, C. E., & Jupp, P. E. 2000, ApJ, 529, 554
Pedregosa, F., Varoquaux, G., Gramfort, A., et al. 2011, JMLR, 12, 2825
Qi, Y., Huang, Z., Xia, L., et al. 2022, A&A, 657, A118
Raouafi, N. E., Patsourakos, S., Pariat, E., et al. 2016, SSRv, 201, 1
Roy, S., Prasad, A., Ghosh, K., Panja, S. C., & Patra, S. N. 2020, SoPh, 295, 100
Scherrer, P., Amezcua, A., & Richard, B. 2010, AGU Fall Meeting, 2010, SH23C−1867
Shen, Y., Liu, Y., Su, J., & Deng, Y. 2012, ApJ, 745, 164
Shibata, K., Ishido, Y., Acton, L. W., et al. 1992, PASJ, 44, L173
Shibata, K., Nakamura, T., Matsumoto, T., et al. 2007, Sci, 318, 1591
Shibayama, T., Maehara, H., Notsu, S., et al. 2013, ApJS, 209, 5
Solanki, S., & Krivova, N. 2011, Sci, 334, 916
The SunPy Community, Barnes, W. T., Bobra, M. G, et al. 2020, ApJ, 890, 68
Torrence, C., Compo, G. P., et al. 1998, BAMS, 79, 61
Tsiropoula, G., Tziotziou, K., Kontogiannis, I., et al. 2012, SSRv, 169, 181
VanderPlas, J. T., & Ivezić, Ž. 2015, ApJ, 812, 18
Virtanen, P., Gommers, R., Oliphant, T. E., et al. 2020, NatMe, 17, 261
Wang, Y. M., & Sheeley, N. R. J. 2002, ApJ, 575, 542
Warwick, C. S. 1966, ApJ, 145, 215
Zaqarashvili, T. V., Albekioni, M., Ballester, J. L., et al. 2021, SSRv, 217, 15